Current-Source-Mode DC-DC Converter With Ripple-Based Control: Concept, Modeling and Duality Principle

Lunbo Deng, *Member, IEEE*, and Guohua Zhou, *Senior Member, IEEE*

***Abstract*—The fundamental current-source-mode (CSM) dc–dc converters and their corresponding power conversion systems have been proposed as effective solutions for constant current drive applications. However, the full potential of CSM converters remains largely untapped due to the lack of advanced control strategies. Widely adopted ripple-based control methods for voltage-source-mode (VSM) dc–dc converters can provide valuable control references for CSM converters. This article revisits the derivation of CSM converters and proposes a ripple-based control for CSM converters (denoted as I^2 control), leveraging the circuit duality principle. Through frequency-domain modeling based on describing function, this article reveals the duality between I^2 control for CSM converters and the well-known V^2 control for VSM converters, highlighting their stability regions in terms of the duty cycle and circuit parameters. Experimental results validate the stability region of I^2 control and demonstrate its significantly faster dynamic response compared to the control methods without ripple information, for example, proportional-integral control and model predictive control.**

***Index Terms*—Current-source-mode (CSM) converter, duality principle, I^2 control, modeling, ripple control, stability, V^2 control, voltage-source-mode (VSM) converter.**

I. INTRODUCTION

DC–DC converters play a crucial role in modern power conversion systems. Among them, voltage-source-mode (VSM) converters have become dominant in both constant voltage and constant current output applications. However, in multichannel current output scenarios, such as driving light-emitting diode (LED) strings, VSM converters face considerable cross-regulation issues [1]. Dong et al. creatively applied current-source-mode (CSM) buck converters to achieve independent dimming of LED strings without cross-regulation [2]. As a result, CSM converters have regained attention, despite the concept of the CSM buck converter having been proposed over a decade ago [3]. A typical CSM power conversion system [4] is shown in Fig. 1(a), while Fig. 1(b) presents the VSM counterpart for comparison. Fig. 1 clearly illustrates the duality between the CSM and VSM power conversion systems, and the exploration of duality principles serves as the central theme and focus of this article.

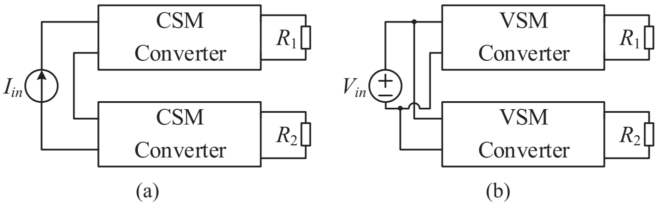

Fig. 1. Power conversion system. (a) Current-source-mode. (b) Voltage-source-mode.

Typical applications high-precision current regulation include LED [5] and laser drivers, welding equipment, and electromagnets [6], where precise and fast current regulation is critical. It is a challenge to achieve constant current supply in VSM converters without additional circuit modifications [7] or specific control strategies [8]. Hence, strategies based on CSM converters provide a promising solution for current regulation.

Research on CSM converters has focused on the development of new topologies, systematic structures, modeling, and control methods. By replacing existing circuit cells, CSM boost, buck-boost, and SEPIC converters are derived, which are essentially variants of the VSM buck, Ćuk, and Zeta converter, respectively [9]. Sun and Cheng [10] summarize that a large proportion of VSM converters are based on switching-inductor and capacitor filter, while CSM converters rely on switching-capacitor and inductor filter. Based on this concept, three switching-capacitor converters are proposed for high current gain applications. Following this, a CSM bidirectional converter is proposed, addressing the gap in bidirectional power flow for CSM converters [11]. Additionally, by introducing a resonant unit, a CSM converter with soft-switching properties is proposed to improve efficiency [12].

The typical structures of single-input-multiple-output and multiple-input-multiple-output power conversion system are voltage-in-voltage-out [13] or voltage-in-current-out [14]. According to the duality principle, the current-in-voltage-out (CIVO) and current-in-current-out (CICO) structures are derived by replacing the common voltage bus with a common current bus [15]. CSM converters in the CICO structure has been reported for

---

Received 24 March 2025; revised 3 June 2025; accepted 12 July 2025. Date of publication 15 July 2025; date of current version 22 October 2025. This work was supported by the National Natural Science Foundation of China under Grant 62271417. Recommended for publication by Associate Editor G. Moschopoulos. *(Corresponding author: Guohua Zhou.)*

The authors are with the School of Electrical Engineering, Southwest Jiaotong University, Chengdu 611756, China (e-mail: denglb_pece@my.swjtu.edu.cn; eeghzhou@swjtu.edu.cn).

Color versions of one or more figures in this article are available at https://doi.org/10.1109/TPEL.2025.3589445.

Digital Object Identifier 10.1109/TPEL.2025.3589445

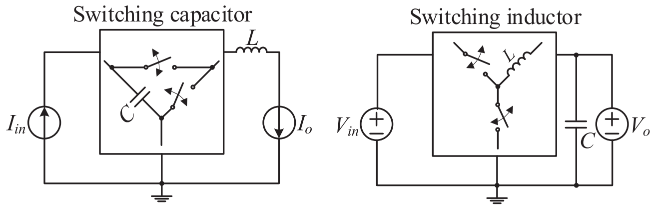

(a) (b)

Fig. 2. Duality principle in topology. (a) Current-source-mode. (b) Voltage-source-mode.

use in LED dimming applications [16], while CSM converters in CIVO structure can be applied in photovoltaic (PV) systems, where the PV module is modeled as a current source with internal resistance [17].

For fundamental CSM converters, the state-space average method consistently yields a very accurate small-signal model of the power stage, which forms the basis for closed-loop controller design [18]. To enhance the dynamic performance, advanced control methods, such as model predictive control (MPC) [19], have been explored for use in CSM converters, However, for low-cost applications, the computational burden of MPC significantly increases the cost of the control chip. In fact, VSM converters offer a wealth of ripple-based control references [20], but these have not received sufficient attention in CSM converters due to the neglect of the duality principle for control methods. Since the state-space average method ignores ripple information, modeling ripple-based control becomes an additional challenge [21]. Furthermore, addressing potential subharmonic oscillation instabilities relies on accurate modeling.

In this article, the ripple-based control method for CSM converters is first introduced. The main contribution is that this article reveals the control duality between CSM converters and VSM converters, providing an important guideline for transferring VSM converter control methods to CSM converters.

The rest of this article is organized as follows. Section II revisits the properties of fundamental CSM converters, including topologies and gains. Section III proposes I^2 control for CSM converters, which serves as the counterpart to V^2 control for VSM converters. Using the describing function (DF) modeling method, the duality principle in frequency-domain characteristics, subharmonic oscillations and circuit parameter selection are discussed. Section IV presents experimental results that validate the stability region of I^2 control and demonstrate its significantly faster dynamic response compared to the control method without ripple information (e.g., PI control and MPC). Section V provides a detailed discussion of I^2 control, including comparison with existing control methods, robustness and applications in other CSM topologies. Finally, Section VI concludes this article.

II. Time-Domain Characteristics of CSM Converters

Fig. 2 illustrates the duality principle between fundamental topologies of VSM and CSM converters. In Fig. 2(a), a storage inductor and two switches arranged in a star connection form the voltage conversion unit for VSM converters. In contrast, a storage capacitor and two switches arranged in a delta connection form the current conversion unit for CSM converters.

TABLE I
Fundamental Topologies of CSM/VSM Converters and Their Current/Voltage Gain

	CSM	VSM
Buck	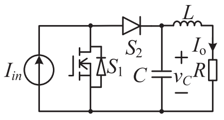 $M_i = 1 - D$	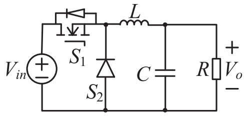 $M_v = D$
Boost	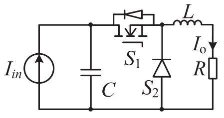 $M_i = 1/D$	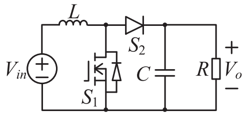 $M_v = 1/(1 - D)$
Buck-boost	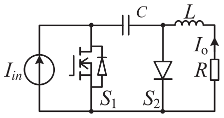 $M_i = (1 - D)/D$	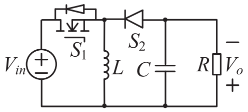 $M_v = D/(1 - D)$

Table I gives the topologies of CSM converters and their VSM counterparts, excluding the equivalent series resistance (ESR) in all capacitor paths. Taking the CSM buck converter as an example, when switch S_1 turns OFF and S_2 turns ON, capacitor voltage v_C is charged, while when S_1 turns ON and S_2 turns OFF, v_C is discharged. Let T_{sw} and D represent the switching period and duty cycle, respectively. Then, the ampere-second balance of v_C can be expressed as

$$I_{\mathrm{o}} D T_{\mathrm{sw}} = (I_{\mathrm{in}} - I_{\mathrm{o}})(1 - D) T_{\mathrm{sw}} \tag{1}$$

the current gain M_i of the CSM buck converter in continuous conduction mode (CCM) is given by

$$M_i = I_{\mathrm{o}}/I_{\mathrm{in}} = 1 - D. \tag{2}$$

Other current gains of CSM converters can be derived in the same way. For VSM converters, the volt-second balance of inductor current leads to voltage gains $M_v = V_{\mathrm{o}}/V_{\mathrm{in}}$ in CCM, which are also given in Table I. Clearly, there is a duality between M_i and M_v, which can be interchanged by replacing D with 1 - D.

The output ripple ratios of CSM and VSM buck converters can be calculated as follows:

$$\frac{\Delta i_{\mathrm{o}}}{I_{\mathrm{in}}} \approx \begin{cases} \frac{D(1-D)T_{\mathrm{sw}}^2}{8LC} & R_{\mathrm{e}} \approx 0 \\ \frac{D(1-D)T_{\mathrm{sw}}R_{\mathrm{e}}}{C} & R_{\mathrm{e}} \gg 0 \end{cases} \tag{3}$$

$$\frac{\Delta v_{\mathrm{o}}}{v_{\mathrm{in}}} \approx \begin{cases} \frac{D(1-D)T_{\mathrm{sw}}^2}{8LC} & R_{\mathrm{e}} \approx 0 \\ \frac{D(1-D)T_{\mathrm{sw}}R_{\mathrm{e}}}{L} & R_{\mathrm{e}} \gg 0 \end{cases} \tag{4}$$

where R_{e} is the ESR in the capacitor paths. The output ripple ratios of CSM and VSM converters can be interchanged by swapping L and C.

This section explores the duality principle in topology, gain and ripple. The duality principle will form the foundation for ripple-based control in CSM converters.

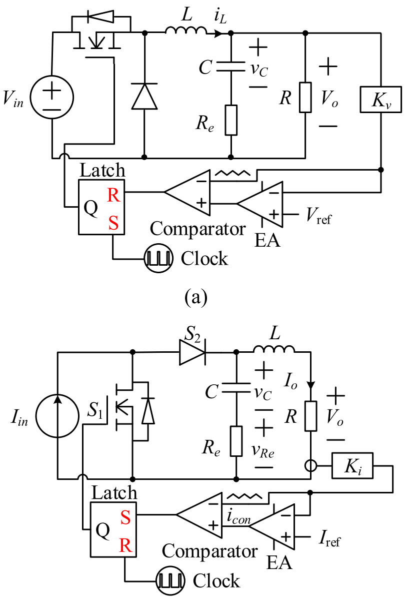

(a)

(b)

Fig. 3. Ripple-based control. (a) V^2 control. (b) I^2 control.

III. FREQUENCY-DOMAIN CHARACTERISTICS OF RIPPLE-BASED CONTROL FOR CSM CONVERTERS

A. Concept of I^2 Control

VSM converters offer a wide range of ripple-based control methods to enhance dynamics or disturbance rejection, such as constant-frequency peak current-mode control, valley current-mode control [22], and V^2 control [23]. Among these, V^2 control has a slow outer voltage loop for reference tracking and a fast inner voltage ripple loop for dynamic performance enhancement. As shown in Fig. 3(a), the output voltage consists of both v_C (related to inductor current i_L) and ESR voltage, V^2 control exhibits the performance and limitations of current-mode control. Furthermore, while ESR improves load dynamics, it also introduces additional stability concerns [24].

In this section, I^2 control is proposed for CSM converters, with its concept illustrated in Fig. 3(b). Tough not shown in Fig. 3(b), the current sampling can be realized using a shunt resistor and a high-precision operational amplifier (Op-Amp) to preserve ripple information. Assume that I^2 control operates in a nonoscillatory case. When the clock signal initiates a new switching period, S_1 turns OFF and S_2 turns ON, simultaneously $K_i i_{\mathrm{o}}$ increases from its initial value, where K_i is the current sampling coefficient. Once $K_i i_{\mathrm{o}}$ reaches the control signal i_{con}, S_1 turns ON and S_2 turns OFF, $K_i i_{\mathrm{o}}$ decreases until the next clock signal arrives. The i_{con} is typically generated by an error amplifier (EA) for output error compensation and dynamic adjustment. By introducing output current ripple into the control loop, it is expected that I^2 control exhibit transient performance similar to that of V^2 control.

It is well known that V^2 control suffers from subharmonic oscillations due to a large duty cycle and small ESR [25]. Therefore, based on the duality principle, it can be anticipated that I^2 control may encounter the same issues. Fig. 4 provides an example showing that when $I_{\mathrm{in}} = 1$ A and I_{o} exceeds 0.5 A, the subharmonic oscillation clearly occurs. The stability region will be explained using a frequency-domain model based on the DF modeling method.

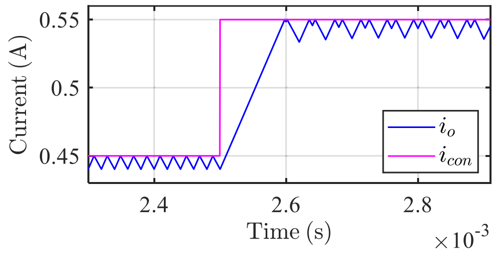

Fig. 4. Subharmonic oscillation in the CSM buck converter.

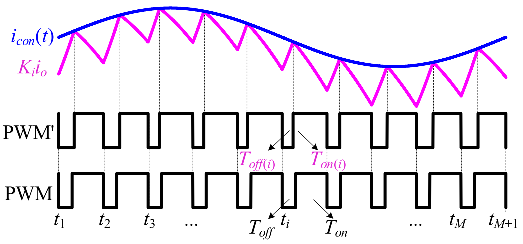

Fig. 5. Perturbed waveform with DF modeling method.

B. Modeling of I^2 Control

A small sinusoidal perturbation with frequency f_{m} is injected into the control signal i_{con}. f_{m} and the switching frequency f_{sw} satisfy the relation $Nf_{\mathrm{sw}} = Mf_{\mathrm{m}}$, where N and M are positive integers [23]. Following the control law, the duty cycle and waveforms are shown in Fig. 5, where PWM' represents the perturbated pulsedwidth modulation signal, while PWM represents the steady-stable counterpart.

The perturbed control signal $i_{\mathrm{con}}(t)$ is expressed as $I_{\mathrm{con}} + \hat{r}(t) = I_{\mathrm{con}} + \hat{r} \cdot \sin(\omega_{\mathrm{m}} t)$, where I_{con} is the steady-state value, $\hat{r}(t)$ is the sinusoidal perturbation, ^ represents small signal, and $\omega_{\mathrm{m}} = 2\pi f_{\mathrm{m}}$. Based on the control law, it is found that

$$\begin{aligned}
&\left[i_{\mathrm{con}}(t_i + T_{\mathrm{off}(i)}) - i_{\mathrm{con}}(t_{i-1} + T_{\mathrm{off}(i-1)})\right] \\
&- \left[i_{\mathrm{con}}(t_{i-1} + T_{\mathrm{off}(i-1)}) - i_{\mathrm{con}}(t_{i-2} + T_{\mathrm{off}(i-2)})\right] \\
&= \frac{K_i}{L}\left(\underbrace{\int\limits_{t_{i-1}+T_{\mathrm{off}(i-1)}}^{t_i+T_{\mathrm{off}(i)}} \hat{v}_C(t)dt - \int\limits_{t_{i-2}+T_{\mathrm{off}(i-2)}}^{t_{i-1}+T_{\mathrm{off}(i-1)}} \hat{v}_C(t)dt}_{a}\right) \\
&+ \frac{K_i}{L}\left(\underbrace{\int\limits_{t_{i-1}+T_{\mathrm{off}(i-1)}}^{t_i+T_{\mathrm{off}(i)}} \hat{v}_{R_{\mathrm{e}}}(t)dt - \int\limits_{t_{i-2}+T_{\mathrm{off}(i-2)}}^{t_{i-1}+T_{\mathrm{off}(i-1)}} \hat{v}_{R_{\mathrm{e}}}(t)dt}_{b}\right)
\end{aligned}$$

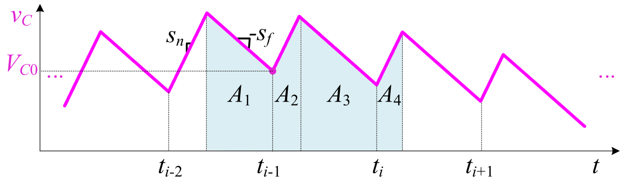

Fig. 6. Perturbed waveform of v_C.

$$-\frac{K_i}{L}\left(\underbrace{\int\limits_{t_{i-1}+T_{\text{off}(i-1)}}^{t_i+T_{\text{off}(i)}}\hat{v}_{\text{o}}(t)dt-\int\limits_{t_{i-2}+T_{\text{off}(i-2)}}^{t_{i-1}+T_{\text{off}(i-1)}}\hat{v}_{\text{o}}(t)dt}_{c}\right). \tag{5}$$

Fig. 6 shows the illustration for calculating a. Assume that $v_C(t_{i\text{-}1}) = V_{C0}$, so the areas A_1 to A_4 can be expressed as

$$\begin{aligned}
A_1 &= V_{C0}T_{\text{on}(i-2)} + s_{\text{f}}T^2_{\text{on}(i-2)}/2\\
A_2 &= V_{C0}T_{\text{off}(i-1)} + s_{\text{n}}T^2_{\text{off}(i-1)}/2\\
A_3 &= \left(V_{C0}+s_{\text{n}}T_{\text{off}(i-1)}-s_{\text{n}}T_{\text{on}(i-1)}\right)T_{\text{off}(i-1)}+s_{\text{f}}T^2_{\text{on}(i-1)}/2\\
A_4 &= \left(V_{C0}+s_{\text{n}}T_{\text{off}(i-1)}-s_{\text{n}}T_{\text{on}(i\text{-}1)}\right)T_{\text{off}(i-1)}+s_{\text{n}}T^2_{\text{off}(i)}/2
\end{aligned} \tag{6}$$

where $s_{\text{n}} = (I_{\text{in}}\text{-}I_{\text{o}})/C$, and $s_{\text{f}} = I_{\text{o}}/C$. Then, a is expressed as

$$\begin{aligned}
a &= A_4 + A_3 - A_2 - A_1\\
&\approx s_{\text{n}}T_{\text{off}}\Delta T_{\text{off}(i)} + (s_{\text{f}}T_{\text{off}} + s_{\text{n}}T_{\text{on}})\Delta T_{\text{off}(i-1)}\\
&\quad + s_{\text{f}}T_{\text{on}}\Delta T_{\text{off}(i-2)}
\end{aligned} \tag{7}$$

where $\Delta T_{\text{off}(i)} = T_{\text{off}(i)} - T_{\text{off}}$.

Similarly, b and c can be calculated as follows:

$$\begin{aligned}
b = R_{\text{e}}I_{\text{in}}\big(&D\Delta T_{\text{off}(i)} + (1-2D)\Delta T_{\text{off}(i-1)}\\
&-(1-D)\Delta T_{\text{off}(i-2)}\big)
\end{aligned} \tag{8}$$

$$\begin{aligned}
c &\approx \frac{R}{K_i}\left(\int\limits_{t_{i-1}+T_{\text{off}(i-1)}}^{t_i+T_{\text{off}(i)}}\hat{r}(t)dt-\int\limits_{t_{i-2}+T_{\text{off}(i-2)}}^{t_{i-1}+T_{\text{off}(i-1)}}\hat{r}(t)dt\right)\\
&= \frac{R}{\omega_{\text{m}}K_i}\left[\hat{r}\left(t_{i-1}+T_{\text{off}(i-1)}+\frac{\pi/2}{\omega_{\text{m}}}\right)\right.\\
&\quad\left.-\hat{r}\left(t_i+T_{\text{off}(i)}+\frac{\pi/2}{\omega_{\text{m}}}\right)\right]\\
&\quad-\frac{R}{\omega_{\text{m}}K_i}\left[\hat{r}\left(t_{i-2}+T_{\text{off}(i-2)}+\frac{\pi/2}{\omega_{\text{m}}}\right)\right.\\
&\quad\left.-\hat{r}\left(t_{i-1}+T_{\text{off}(i-1)}+\frac{\pi/2}{\omega_{\text{m}}}\right)\right].
\end{aligned} \tag{9}$$

Letting $\Delta T_{\text{off}(i-2)} = \Delta T_{\text{off}(i-1)}e^{-j\omega_{\text{m}}T_{\text{sw}}} = \Delta T_{\text{off}(i)}e^{-j2\omega_{\text{m}}T_{\text{sw}}}$ and combining (5)–(9), $\Delta T_{\text{off}(i)}$ can be express as (12), as shown at the bottom of this page.

The small-signal perturbation on the PWM signal $d(t)$ can be expressed as

$$\hat{d}(t)|_{0\le t\le t_{M+1}} = -\sum_{i=1}^{M}\left[u\left(t-t_i-T_{\text{off}}\right)-u\left(t-t_i-T_{\text{off}(i)}\right)\right] \tag{10}$$

where $u(t) = 1$ when $t > 0$. Then, Fourier analysis is performed on $\hat{d}(t)$

$$C_{\text{m}}(\hat{d}) = \frac{f_{\text{m}}}{N}\int\limits_0^{T_{M+1}}\hat{d}(t)e^{-j\omega_{\text{m}}t}dt. \tag{11}$$

The Fourier coefficient of $\hat{r}(t)$ is $\hat{r}/2j$. Therefore, the DF of I^2 controller, from the control signal to the PWM signal, can be expressed as

$$\frac{C_{\text{m}}\left(\hat{d}(t)\right)}{C_{\text{m}}\left(\hat{r}(t)\right)} = \frac{-f_{\text{sw}}\left(1-e^{-j\omega_{\text{m}}T_{\text{sw}}}\right)^2\left(1+\frac{R}{jL\omega_{\text{m}}}\right)}{\frac{K_i}{L}\left(\alpha_0+\alpha_1e^{-j\omega_{\text{m}}T_{\text{sw}}}+\alpha_2e^{-j2\omega_{\text{m}}T_{\text{sw}}}\right)} \tag{13}$$

where

$$\begin{aligned}
\alpha_0 &= s_{\text{n}}T_{\text{off}} + DI_{\text{in}}R_{\text{e}}\\
\alpha_1 &= s_{\text{f}}T_{\text{off}} + s_{\text{n}}T_{\text{on}} + (1-2D)I_{\text{in}}R_{\text{e}}\\
\alpha_2 &= s_{\text{f}}T_{\text{on}} - (1-D)I_{\text{in}}R_{\text{e}}.
\end{aligned} \tag{14}$$

By replacing $j\omega_{\text{m}}$ with s in (13), the transfer function of I^2 controller $\hat{d}(s)/\hat{i}_{\text{con}}(s)$ is obtained. Then, the control-to-output-current transfer function can be expressed as

$$\begin{aligned}
\frac{\hat{i}_{\text{o}}(s)}{\hat{i}_{\text{con}}(s)} &= -\frac{\hat{d}(s)}{\hat{i}_{\text{con}}(s)}\cdot\frac{I_{\text{in}}}{Cs}\cdot\frac{\frac{R_{\text{e}}}{1/sC}+1}{sL+R}\\
&= \frac{I_{\text{in}}f_{\text{sw}}\left(sCR_{\text{e}}+1\right)\left(1-e^{-sT_{\text{sw}}}\right)^2}{K_iCs^2\left(\alpha_0+a_1e^{-sT_{\text{sw}}}+a_2e^{-2sT_{\text{sw}}}\right)}.
\end{aligned} \tag{15}$$

By introducing a small output voltage perturbation, the output-voltage-to-output-current transfer function (output admittance) is derived. Similarly, by introducing a small input current perturbation, the input-current-to-output-current transfer function (audio susceptibility) is derived. They are expressed as follows:

$$\frac{\hat{i}_{\text{o}}(s)}{\hat{v}_{\text{o}}(s)} = \frac{\frac{I_{\text{in}}f_{\text{sw}}\left(1-e^{-sT_{\text{sw}}}\right)^2(sCR_{\text{e}}+1)}{Cs^2(\alpha_0+a_1e^{-sT_{\text{sw}}}+a_2e^{-2sT_{\text{sw}}})}-1}{sL} \tag{16}$$

$$\begin{aligned}
\frac{\hat{i}_{\text{o}}(s)}{\hat{i}_{\text{in}}(s)} &= \left[1-D-\frac{I_{\text{in}}f_{\text{sw}}\left(1-e^{-sT_{\text{sw}}}\right)\left(1-e^{-sT_{\text{off}}}\right)\left(\frac{1}{sC}+R_{\text{e}}\right)}{s\left(\alpha_0+a_1e^{-sT_{\text{sw}}}+a_2e^{-2sT_{\text{sw}}}\right)}\right]\\
&\quad\times\frac{\frac{1}{sC}+R_{\text{e}}}{sL+R}.
\end{aligned} \tag{17}$$

$$\Delta T_{\text{off}(i)} = \frac{\hat{r}\sin\omega_{\text{m}}\left(t_i+T_{\text{off}(i)}\right)\left(1-e^{-j\omega_{\text{m}}T_{\text{sw}}}\right)^2\left(1+\frac{R}{jL\omega_{\text{m}}}\right)}{\frac{K_i}{L}\left[(s_{\text{n}}T_{\text{off}}+DI_{\text{in}}R_{\text{e}})+(s_{\text{f}}T_{\text{off}}+s_{\text{n}}T_{\text{on}}+(1-2D)I_{\text{in}}R_{\text{e}})e^{-j\omega_{\text{m}}T_{\text{sw}}}+\left(s_{\text{f}}T_{\text{on}}-(1-D)I_{\text{in}}R_{\text{e}}\right)e^{-j2\omega_{\text{m}}T_{\text{sw}}}\right]} \tag{12}$$

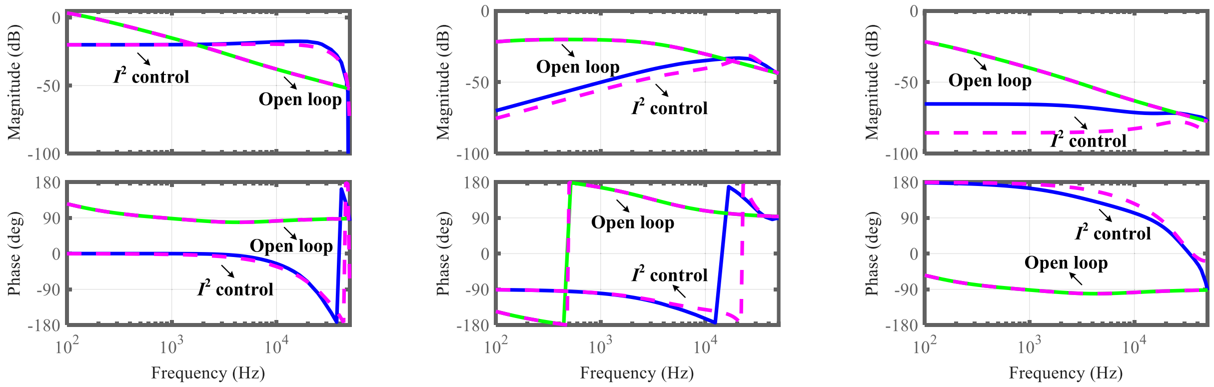

(a) (b) (c)

Fig. 7. Bode plots of transfer functions. (a) $\hat{i}_\mathrm{o}(s)/\hat{i}_\mathrm{con}(s)$ for I^2 control and $\hat{i}_\mathrm{o}(s)/\hat{d}(s)$ for open loop. (b) Output admittance for I^2 control and open loop. (c) Audio susceptibility for I^2 control and open loop.

TABLE II
CIRCUIT PARAMETERS

Parameters	Symbol	Value
Switch frequency	f_sw	50 kHz
Input current	I_in	1–4 A
Output current	I_o	350 mA
Sampling gain	K_i	10
Capacitance	C	220 µF
Inductance	L	500 µH
Load voltage	V_o	2.8 V
Shunt resistance	R	1 Ω

With the circuit parameters listed in Table II, Fig. 7 shows the Bode plots of $\hat{i}_\mathrm{o}(s)/\hat{i}_\mathrm{con}(s)$, output admittance and audio susceptibility, where the solid lines represent the theoretical transfer functions, and the dashed lines represent the frequency-sweeping results obtained using SIMPLIS simulation. As given in Fig. 7(a), the theoretical control-to-output-current transfer function matches the simulation well, which is critical for stability analysis. The discrepancies in Fig. 7(b) and (c) are acceptable, as the output admittance and audio susceptibility are intended for qualitative comparison.

Moreover, Fig. 7(a) also includes open-loop Bode plot of $\hat{i}_\mathrm{o}(s)/\hat{d}(s)$, Fig. 7(b) includes open-loop output admittance, and Fig. 7(c) includes open-loop audio susceptibility. Since open-loop transfer functions can be derived through the common state-space average modeling method [26], the modeling processes are omitted. The corresponding transfer functions of open loop are shown as

$$\left.\frac{\hat{i}_\mathrm{o}(s)}{\hat{d}(s)}\right|_{\text{open loop}} = -\frac{I_\mathrm{in}(sCR_\mathrm{e}+1)}{s^2LC+sC(R+R_\mathrm{e})+1} \tag{18}$$

$$\left.\frac{\hat{i}_\mathrm{o}(s)}{\hat{v}_\mathrm{o}(s)}\right|_{\text{open loop}} = \frac{-sC}{s^2LC+sC(R+R_\mathrm{e})+1} \tag{19}$$

$$\left.\frac{\hat{i}_\mathrm{o}(s)}{\hat{i}_\mathrm{in}(s)}\right|_{\text{open loop}} = \frac{(1-D)(sCR_\mathrm{e}+1)}{s^2LC+sC(R+R_\mathrm{e})+1}. \tag{20}$$

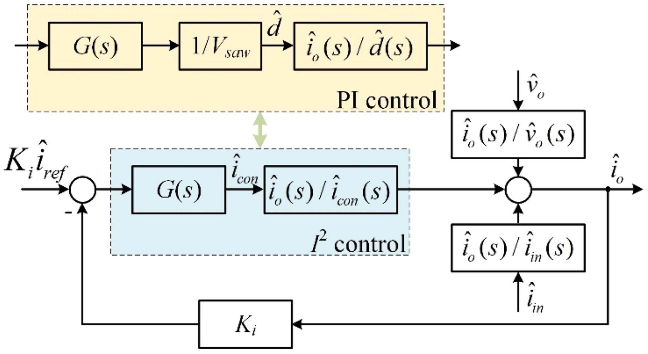

Fig. 8. Small-signal control block diagram for PI control and I^2 control.

C. Loop Design

Fig. 8 depicts the small-signal control block diagram for PI control and I^2 control, where $G(s)$ is the transfer function of EA, $V_\mathrm{saw} = 15$ V denotes the magnitude of sawtooth signal. When $I_\mathrm{in} = 2.5$ A (the midpoint of input current) and $I_\mathrm{in} = 350$ mA (a typical LED driving current), $R = 1\ \Omega$ (ignoring the resistor on LED and considering the shunt resistor), the phase margin (PM) and gain margin (GM) of loop gain $T(s)$ are required larger than 45° and 10 dB, respectively. Finally, the EA for PI control is designed as -(8.2 + 3030/s), the negative sign is included to offset the negative sign in (18), whereas the EA for I^2 control is 30303/s.

Fig. 9(a) depicts the Bode plot of $T(s)$, and Fig. 9(b), and (c) depicts the closed-loop output admittance and audio susceptibility, respectively. Table III gives the frequency-domain characteristics depicted in Fig. 9. Except for GM, I^2 control demonstrates overall superiority over PI control, including higher crossover frequency, larger PM and loop gain, and lower closed-loop output admittance and audio susceptibility, indicating its faster dynamics and disturbance rejection ability than PI control.

D. Stability of I^2 Control

Although the model (15) is accurate, it is complicated to investigate the stability of I^2 control. For simplicity, Padé approximation is performed on the exponential term [27], as

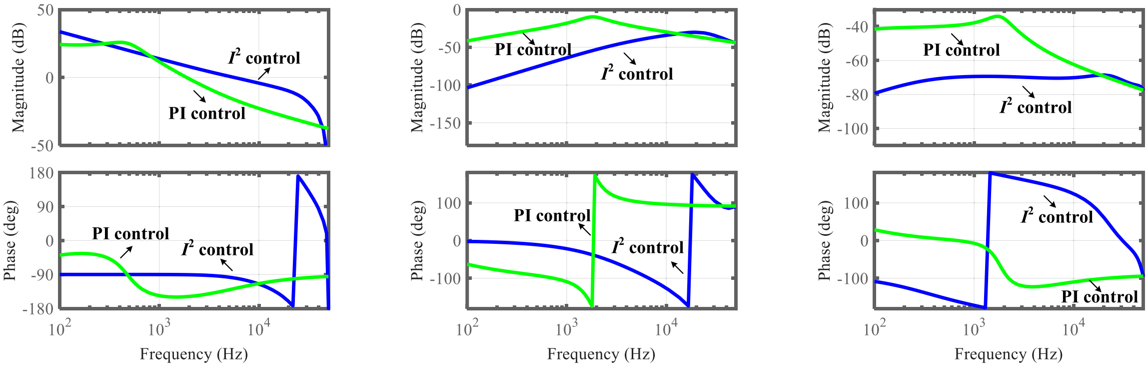

(a) (b) (c)

Fig. 9. Bode plots of closed-loop transfer functions. (a) Loop gain. (b) Closed-loop output admittance. (c) Closed-loop audio susceptibility for I^2 control and open loop.

TABLE III
CLOSED-LOOP FREQUENCY-DOMAIN CHARACTERISTICS

	PI control	I^2 control
Crossover frequency	1.7 kHz	6 kHz
PM	45°	80°
GM	/	10 dB
Loop gain (at 100 Hz)	24 dB	32 dB
Closed-loop output admittance (at 100 Hz)	-40 dB	-100 dB
Closed-loop audio susceptibility (at 100 Hz)	-41 dB	-80 dB

$$e^{-sT_{\mathrm{sw}}} = 1 - \frac{sT_{\mathrm{sw}}}{\frac{s^2}{\omega_1^2}+\frac{s}{Q_1\omega_1}+1} \tag{21}$$

where $Q_1 = 2/\pi$, and $\omega_1 = \pi/T_{\mathrm{sw}}$. Padé approximation can be accurate up to half of the switching frequency. Then, (15) is rewritten as

$$\frac{\hat{i}_{\mathrm{o}}(s)}{\hat{i}_{\mathrm{con}}(s)} = \frac{I_{\mathrm{in}}\left(sCR_{\mathrm{e}}+1\right)}{K_i C f_{\mathrm{sw}}\left(\beta_4 s^4+\beta_3 s^3+\beta_2 s^2+\beta_1 s^1+\beta_0\right)} \tag{22}$$

where

$$\begin{aligned}
\beta_4 &= \frac{\alpha_0+\alpha_1+\alpha_2}{\omega_1^4} > 0,\ \beta_3 = \frac{2\alpha_0-2\alpha_2}{Q_1\omega_1^3} > 0\\
\beta_2 &= \frac{1}{\omega_1^2}\left(2\alpha_0+2\alpha_1+2\alpha_2+\frac{\alpha_0-\alpha_1+\alpha_2}{Q_1^2}\right) > 0\\
\beta_1 &= \frac{2\alpha_0-2\alpha_2}{Q_1\omega_1} > 0,\ \beta_0 = \alpha_0+\alpha_1+\alpha_2 > 0.
\end{aligned} \tag{23}$$

According to the Routh–Hurwitz stability criterion, stable I^2 control should satisfy

$$\begin{aligned}
&\beta_i > 0,\ i = 0,\ 1,\ 2,\ 3,\ 4\\
&\qquad \Delta = \beta_3\beta_2\beta_1 - \left(\beta_4\beta_1^2+\beta_3^2\beta_0\right)\\
&\qquad\quad = \frac{4I_{\mathrm{in}}^3R_{\mathrm{e}}^2(2D-1)\left[2CR_{\mathrm{e}}-(2D-1)T_{\mathrm{sw}}\right]}{CQ_1^4\omega_1^6} > 0.
\end{aligned} \tag{24}$$

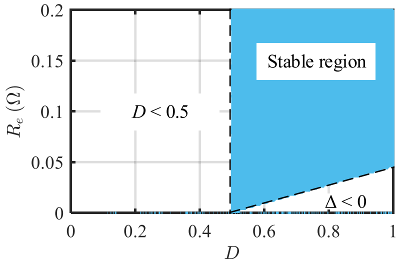

Fig. 10. Stability region of I^2 control.

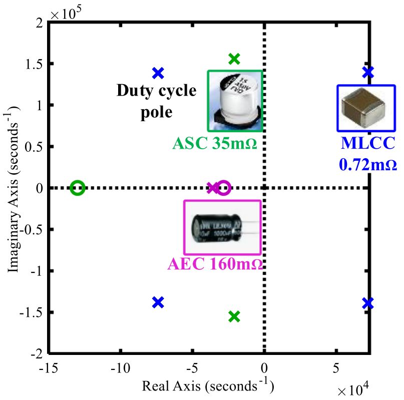

Fig. 11. Pole-zero map of I^2 control for different capacitor types. For clarity, the ESR zero and one AEC pole at much higher frequency are not shown.

Fig. 10 illustrates the stability region, where $\Delta > 0$, i.e., $D > 0.5$ and

$$CR_{\mathrm{e}} > \frac{(2D-1)T_{\mathrm{sw}}}{2}. \tag{25}$$

Similar to other ripple-based constant-frequency controls [28], I^2 control also has a stable boundary at $D = 0.5$. Furthermore, I^2 control requires an appropriate capacitor selection to avoid subharmonic oscillations. Fig. 11 illustrates the pole-zero map of the control-to-output-current transfer function with a fixed duty cycle and different capacitor types: aluminum electrolytic capacitor (AEC), aluminum solid capacitor (ASC), multilayer ceramic capacitor (MLCC). There are two pairs of

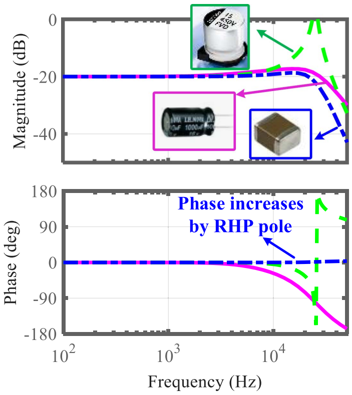

Fig. 12. Bode plot of I^2 control for different capacitor types.

TABLE IV
DUALITY PRINCIPLE OF CSM/VSM BUCK CONVERTERS AND THEIR RIPPLE-BASED CONTROL METHODS

Buck converter	CSM	VSM
Topology	Switching capacitor	Switching inductor
Filter	Inductor	Capacitor
Ripple	(3)	(4)
Gain	$M_i = 1 - D$	$M_v = D$
Control	I^2 control	V^2 control
Stability conditions	$D > 0.5$	$D < 0.5^*$
	$CR_e > \frac{(2D-1)T_{sw}}{2}$	$CR_e > \left(\frac{1}{2} + \frac{D^2}{1-2D}\right)T_{sw}{}^*$

* The stability conditions for V^2 control can be found in [29].

poles in Fig. 11. One pair is fixed, as it is solely related to the duty cycle. As the ESR decreases, the other pair of poles moves from the real axis in left half-plane to the right half-plane (RHP).

In the Bode plot in Fig. 12, the AEC with larger ESR exhibits a lower resonant peak at half of the switching frequency compared to ASC, while the MLCC, with negligible ESR, introduces RHP poles and instability. Hence there is paradox between ripple magnitude and stability for I^2 control. The designer can select an appropriate capacitor based on (3) and (25).

E. Summary of Duality Principle

Table IV gives the duality principle of CSM/VSM buck converters. Clearly CSM converters and their ripple-based control exhibit strong similarities to their VSM counterparts. Although additional CSM control techniques, such as slope compensation, variable-frequency control, are not discussed in this article, it can be anticipated that they will also exhibit a strong duality with VSM converters. This provides an excellent foundation for transplanting VSM converter control techniques to CSM converters.

IV. EXPERIMENTAL RESULTS

This section verifies the transient performance and stability conditions of the I^2-controlled CSM buck converter, in comparison with PI control, finite-control-set (FCS)-MPC, and continuous-control-set (CCS)-MPC. The experimental setup is shown in Fig. 13, and the corresponding circuit parameters are listed in Table II. Further details regarding MPC are provided in the Appendix.

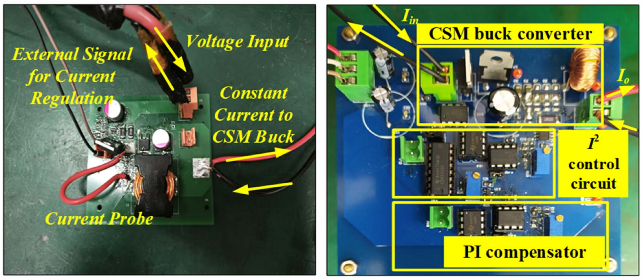

(a) (b)

Fig. 13. Experimental Setup. (a) Current source circuit. (b) CSM buck converter and control circuit.

As shown in Fig. 13(a), the input for the CSM buck converter is provided by a custom-designed adjustable current source based on LM3409, which employs constant off-time control to deliver a stable current supply and enable fast current adjustment. Fig. 13(b) illustrates the CSM buck converter and its control circuit. A Schottky diode (STPS10L60D) and a MOSFET (IRFZ24NPBF), driven by an optocoupler (ICPL3120), form the switching network. The TL431 provides a reference voltage for both control methods. For I^2 control, the output current ripple is sampled using an INA128 (1.3 MHz bandwidth). The EA is an LM318, the comparator is an LM393, the RS latch is a CD4043, and the clock signal is supplied externally by a signal generator. For PI control, the same types of EA and comparator are used, and the sawtooth signal is also provided by an external signal generator. Besides, the MPC is implemented with microcontroller unit (MCU) F280049 from Texas Instruments.

A. Transient Performance

Fig. 14 compares the input response when the input current increases from 1 to 4 A. The reference current is 350 mA, and the load voltage is 2.8 V, which are the typical operating current and voltage of the white LED.

Compared with PI control, the duty cycles of I^2 control and CCS-MPC adjust within a few switching periods, resulting in negligible impact on the output current. FCS-MPC also maintains the average output current at 350 mA. However, the ripple magnitude increases as the equivalent switching frequency decreases. In Fig. 15, where the input current decreases from 4 to 1 A, all control methods exhibit similar dynamic performance as in Fig. 14. However, the ripple magnitude of FCS-MPC decreases as the equivalent switching frequency increases. If only the dynamics of the average output current are considered while ignoring ripple, the dynamic performance (including the output current variation and recovery time) ranks as follows: PI control $<<$ FCS-MPC $\approx$ CCS-MPC $\approx$ I^2 control.

Fig. 16 compares the load response when the load voltage steps up from 1 to 5 V. Due to the sudden increase, the output

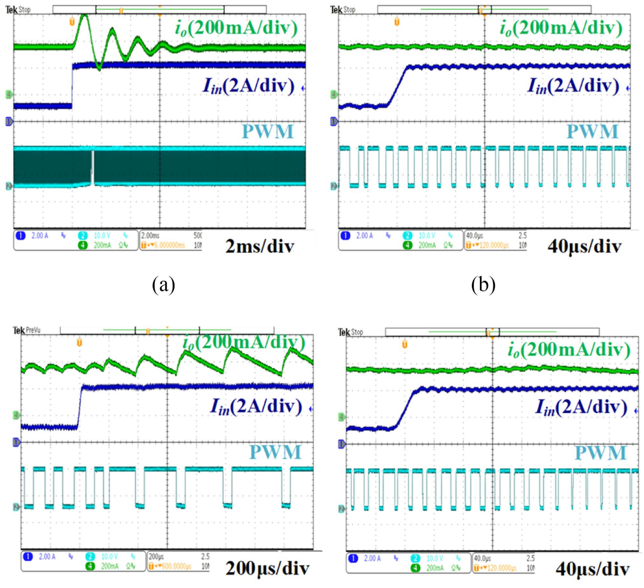

(a) (b)

(c) (d)

Fig. 14. Dynamic response to an input current step-up. (a) PI control. (b) I^2 control. (c) CCS-MPC. (d) FCS-MPC.

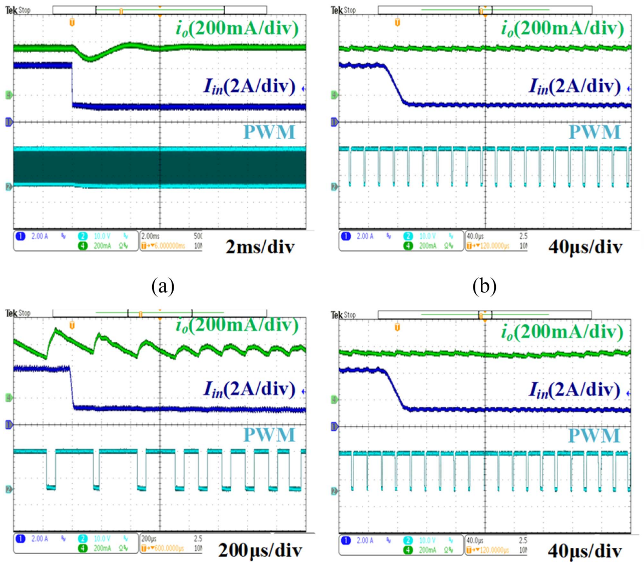

(a) (b)

(c) (d)

Fig. 15. Dynamic response to an input current step-down. (a) PI control. (b) I^2 control. (c) CCS-MPC. (d) FCS-MPC.

current drops sharply to nearly 0 A under PI control and CCS-MPC. However, the recovery time of CCS-MPC is significantly shorter than that of PI control. For I^2 control and FCS-MPC, the output current drops by approximately 200 mA. FCS-MPC recovers faster, while I^2 control exhibits an overshoot caused by the delay of the integrator in the EA. In this load voltage step-up scenario, the magnitude of output current drop ranks as: FCS-MPC $<$ I^2 control $<$ CCS-MPC $\approx$ PI control; the recovery time ranks as: FCS-MPC $<$ CCS-MPC $<$ I^2 control $<<$ PI control.

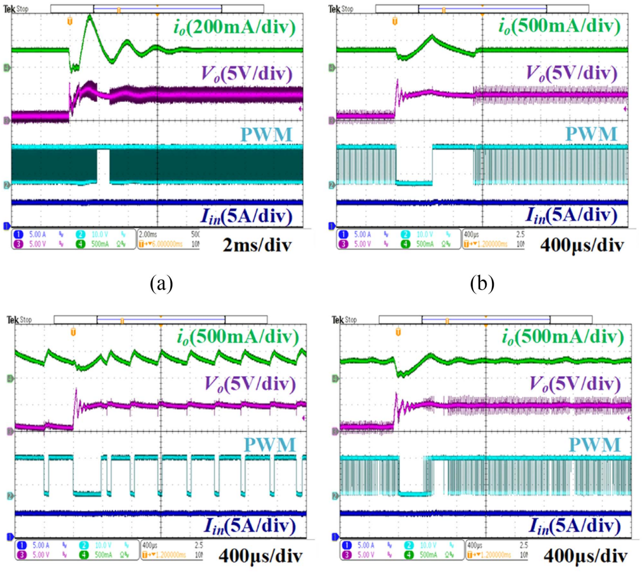

(a) (b)

(c) (d)

Fig. 16. Dynamic response to a load voltage step-up. (a) PI control. (b) I^2 control. (c) CCS-MPC. (d) FCS-MPC.

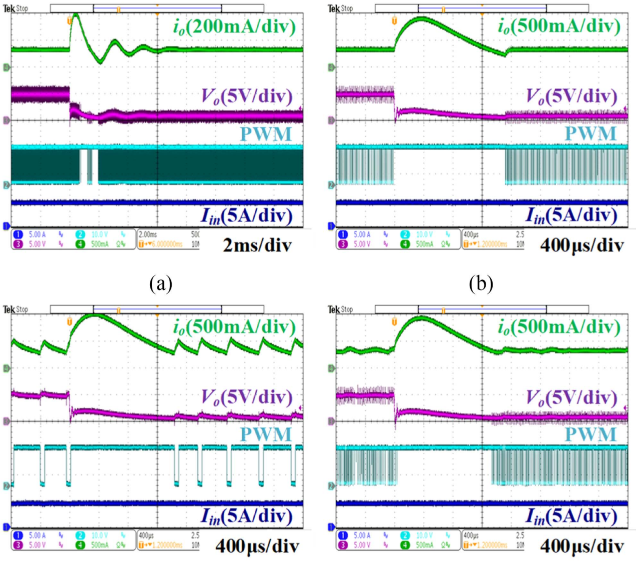

(a) (b)

(c) (d)

Fig. 17. Dynamic response to a load voltage step-down. (a) PI control. (b) I^2 control. (c) CCS-MPC. (d) FCS-MPC.

In Fig. 17, where the load voltage steps down from 5 to 1 V, all control methods except PI control are able to rapidly short-circuit the input current to restore the output current, hence their recovery times are nearly identical. In this voltage step-down scenario, the dynamic performance ranks as follows: PI control $<<$ FCS-MPC $\approx$ CCS-MPC $\approx$ I^2 control.

Fig. 18 compares the start-up dynamic performance of all control methods. The start-up performance ranking is: PI control $<<$ I^2 control $<$ FCS-MPC $\approx$ CCS-MPC.

The experimental results indicate that, FCS-MPC exhibits the best dynamic performance under all test conditions; however, its

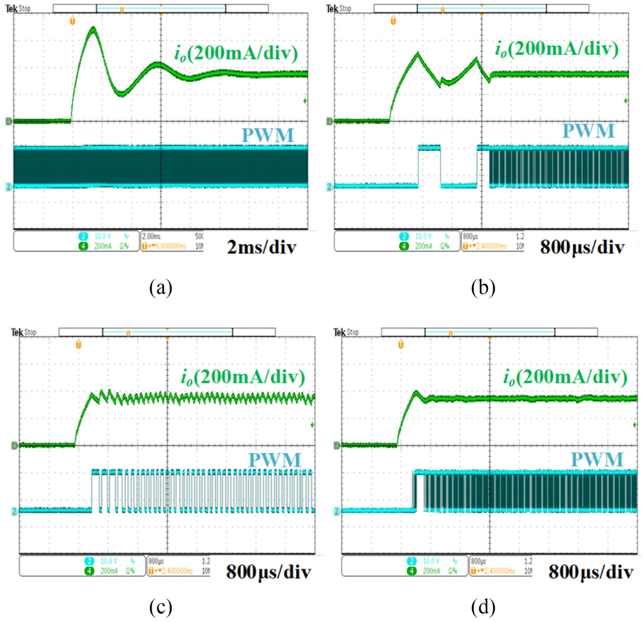

(a) (b) (c) (d)

Fig. 18. Dynamic test during start-up. (a) PI control. (b) I^2 control. (c) CCS-MPC. (d) FCS-MPC.

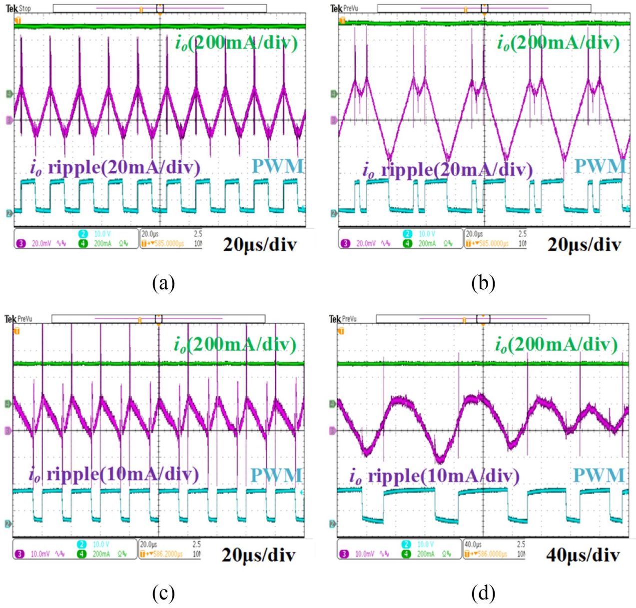

(a) (b) (c) (d)

Fig. 19. Verification of stability issues. (a) $D = 0.51$, $R_e = 0.4$ Ω. (b) $D = 0.49$, $R_e = 0.4$ Ω. (c) $D = 0.7$, $R_e = 20$ mΩ. (d) $D = 0.7$, $R_e = 10$ mΩ.

large ripple may limit its use in precision applications. PI control shows the poorest dynamic performance. I^2 control and CCS-MPC lie between FCS-MPC and PI control, with similar performance in most scenarios. The start-up overshoot of I^2 control can be mitigated by applying soft-start techniques commonly used in switching converters; this aspect is not further discussed in this article. In summary, I^2 control achieves MPC-like dynamic performance with much lower hardware cost. Further discussion of the four control strategies is provided in Section V-A.

B. Stability Issues

Fig. 19 illustrates the impact of parameters on stability. In these experiments, the capacitor branch is replaced with an MLCC and a surface-mounted-device (SMD) resistor in series. The SMD resistor can be adjusted to achieve the desired resistance for the ESR boundary test. Additionally, ac coupling is applied to channel 3 (i_o ripple) in Fig. 19 to observe the output current ripple and determine whether subharmonic oscillation has occurred.

In Fig. 19(a) and (b), the resistance is adjusted to satisfy the stable condition of (25), excluding the impact of ESR. When D is 0.51, the circuit operates normally. However, when D is reduced to 0.49, subharmonic oscillation occurs. These results confirm the stability boundary at $D = 0.5$.

To verify the impact of ESR on stability, the duty cycle is set to 0.7 to eliminate subharmonic oscillations caused by an improper duty cycle. According to (25), the stable boundary of ESR is 18 mΩ. In Fig. 19(c), with the ESR set to 20 mΩ, the circuit operates normally. However, in Fig. 19(d), when the ESR is reduced to 10 mΩ, the circuit enters a state of subharmonic oscillation. These comparative results validate that (25) provides an accurate guide for capacitor selection.

V. DISCUSSION

A. Comparison of PI Control, I^2 Control and MPC

Table V compares the PI control, I^2 control and MPC in terms of cost, complexity and current regulation performance.

In terms of hardware cost, PI control can be realized using a low-cost commercial PWM controller IC (e.g., TL494), which integrates reference and oscillator functions, and is available with just a few cents. In contrast, I^2 control currently lacks dedicated commercial ICs. Apart from the reference and oscillator IC, it requires additional discrete components, such as a high-precision Op-Amp for ripple sampling (e.g., INA310), a comparator (e.g., LM393), and an RS latch (e.g., CD4043). Among these, the high-precision Op-Amp dominates the total cost, and the total cost for I^2 control is approximately \$1. For MPC, an MCU, such as F28035, is required, along with peripheral circuits. The total cost for MPC typically exceeds \$5.

The designs of PI control and I^2 control require only a background in classical control theory. For FCS-MPC, the limited number of switching states ($d \in \{0, 1\}$) makes the design very straightforward. In contrast, the design of CCS-MPC is significantly more complex, as it involves continuous control actions ($d \in [0, 1]$) and requires the knowledge of optimization theory.

The implementation complexity of I^2 control is slightly higher than that of PI control due to the additional hardware components required. The calculation complexity of MPC depends on the prediction horizon. For CCS-MPC, the size of the computation matrix grows linearly with the prediction horizon. In contrast, for FCS-MPC, the computational complexity grows exponentially with the prediction horizon [30].

PI control always exhibits the slowest transient response. Under input and load variations, I^2 control demonstrates dynamic

TABLE V
COMPARISON OF PI CONTROL, I^2 CONTROL AND MPC

		PI control	I^2 control	MPC	
				FCS	CCS
Hardware	Key IC	PWM	High-precision Op-Amp Comparator RS latch	MCU	
	Cost	Low	Medium	High	
Complexity	Design	Low			High
	Implementation	Low	Medium	Depends on the prediction horizon	
Dynamics	Input	Slow	Extremely Fast		
	Load	Slow	Fast		
	Start-up	Slow	Medium	Fast	
Others	Ripple	Good	Medium	Worst	Good
	Limitation	/	Only for high current step-down applications	Unclear small-signal model	

performance comparable to that of MPC. However, its start-up settling time and overshoot are slightly inferior to those of MPC.

It is worth noting that the output current ripple under I^2 control is intentionally designed to be slightly higher than that of PI control and CCS-MPC. This is due to the selection of a larger ESR, which helps ensure system stability but consequently amplifies the ripple. Among all strategies, FCS-MPC exhibits the largest ripple. For example, when $I_{\mathrm{o}}/I_{\mathrm{in}} = 0.2$, the control sequence contains $\{1, 1, 1, 1, 0\}$, yielding an equivalent switching period that is five times longer than the control horizon. This accounts for the variation in ripple observed in Fig. 14(c) and (d) as $I_{\mathrm{o}}/I_{\mathrm{in}}$ changes.

Moreover, I^2 control is applicable primarily in high current step-down applications ($D > 0.5$) to avoid subharmonic oscillations. In contrast, a key limitation of MPC lies in the absence of a clear frequency-domain model, which poses challenges for cascaded stability analysis in two-stage architectures [e.g., Fig. 1(a)].

In conclusion, I^2 control achieves dynamic performance comparable to MPC through analog implementation. Although it is limited in high current step-down applications, the clear and straightforward frequency-domain design enhances its practicality. In cost-sensitive applications, I^2 control offers a significant advantage.

B. Robustness Under Parameter Variation and Noise for I^2 Control

Consider a ±20% variation of C and L due to long-term operation and manufacturing tolerances. The simulation results under output voltage steps are shown in Fig. 20(a). Except for the case where both C and L are at 80% of their nominal values, I^2 control exhibits highly consistent dynamic performance.

The sampling noise is introduced into the control loop, as shown in Fig. 20(b). Although the output current ripple increases with rising noise, the average output current still tracks the reference. This is attributed to the outer current loop of I^2 control, which limits the maximum output current around the reference and is insensitive to noise. This simulation demonstrates that the average current under I^2 control is robust against noise, whereas the ripple is less tolerant.

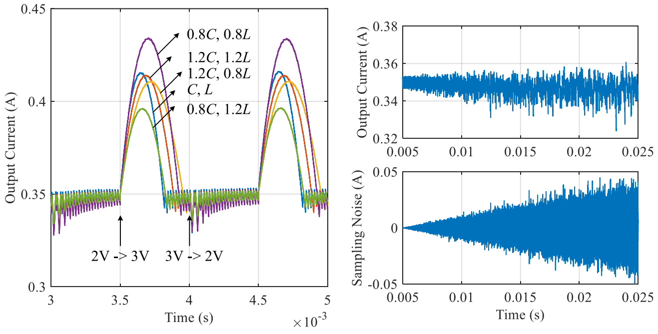

(a) (b)

Fig. 20. Robustness simulation. (a) Against parameter variation. (b) Against noise.

In conclusion, as I^2 control shows robustness under parameter variation and outer loop, the unique challenge is the sensitive of inner current ripple loop. Accurately reconstructing the current ripple requires high-precision Op-Amp, and sampling noise should be minimized as much as possible. For very high-frequency applications, these may significantly increase the cost.

C. Extension to Other CSM Topologies

Fig. 21 depicts the waveform of CSM boost and buck-boost converters with I^2 control. For CSM boost converter, when $I_{\mathrm{in}} = 1$ A and I_{o} exceeds 2 A ($D < 0.5$), the subharmonic oscillation occurs. For CSM buck-boost converter, when $I_{\mathrm{in}} = 1$ A and I_{o} exceeds 1 A ($D < 0.5$), the subharmonic oscillation occurs. The duality principle still holds: $D = 0.5$ remains the boundary for subharmonic oscillation in both CSM and VSM converters.

However, for CSM boost and buck-boost converters, no instability related to ESR is observed in the simulations. This is a difference compared to V^2-controlled VSM boost and buck-boost

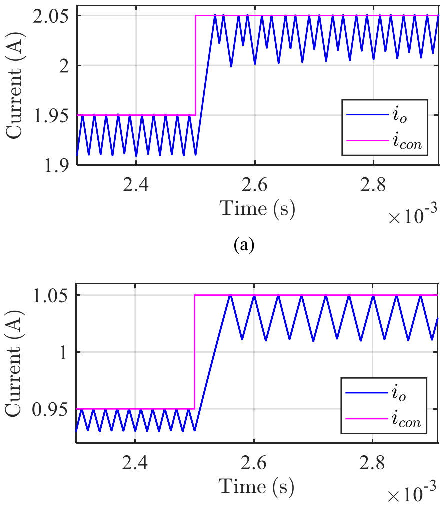

(a)

(b)

Fig. 21. Extension of I^2 control. (a) CSM boost converter. (b) CSM buck-boost converter.

converters, where ESR-related instability has been validated in literatures [31], [32].

VI. CONCLUSION

Based on the duality principle between CSM and VSM converters, this article first proposes a ripple-based control method for CSM converters. Through precise frequency-domain modeling, the inherent duality between I^2 control for CSM converters and V^2 control for VSM converters is revealed, covering both transient performance and stability regions. More importantly, this article provides a valuable approach for transferring VSM control techniques to CSM converters. The duality principle significantly simplifies the design process of CSM converter control, enabling designers to easily evaluate control performance and stability by referencing existing VSM control methods. Through comparison with existing control methods, I^2 control is demonstrated to be a promising scheme for fast current regulation.

APPENDIX

Fig. 22 depicts the control block of MPC for comparison purpose. The control periods for CCS-MPC and FCS-MPC are both set to 20 μs, which are the same as switching period of the CSM buck converter.

For CCS-MPC, the prediction horizon and the control horizon are set to 3 and 1, respectively. The corresponding cost function is expressed as

$$J_{\mathrm{CCS}} = \sum_{j=1}^{3} \left[i_{\mathrm{o}}\left(t+j|t\right) - I_{\mathrm{ref}}\right]^2 + \lambda\left[\Delta di_{\mathrm{in}}\left(t\right)\right]^2 \tag{A1}$$

where λ is a weighting coefficient for tunning a smooth duty cycle variation, and $\Delta di_{\mathrm{in}}(t)$ is the control increment per control period. To achieve a faster response, λ can be set to a low value, i.e., 0.01 in this case.

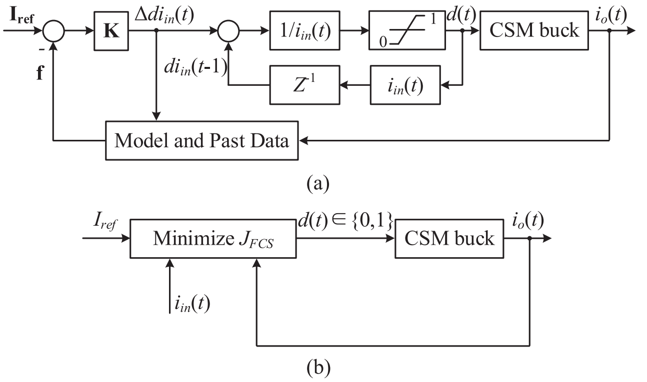

(a)

(b)

Fig. 22. Control block of MPC. (a) CCS-MPC. (b) FCS-MPC.

The model is discrete-time version of

$$\frac{i_{\mathrm{o}}(s)}{d(s)i_{\mathrm{in}}(s)} = -\frac{sCR_{\mathrm{e}}+1}{s^2LC + sC(R+R_{\mathrm{e}})+1} \tag{A2}$$

where $d(t)\times i_{\mathrm{in}}(t)$ forms the new control variable $di_{\mathrm{in}}(t)$ of CCS-MPC, by doing so, the input current variation is introduced. The control variable increment is expressed as

$$\Delta di_{\mathrm{in}}(t) = \mathbf{K}(\mathbf{I_{ref}} - \mathbf{f}) \tag{A3}$$

where $\mathbf{K}$ is the control gain vector, $\mathbf{I_{ref}} = [I_{\mathrm{ref}}\ I_{\mathrm{ref}}\ I_{\mathrm{ref}}]^{\mathrm{T}}$, and $\mathbf{f}$ the free response vector. In the studied case, $\mathbf{K} = [1.82\ 2.08\ 2.33]$, $\mathbf{f}$ is updated in each control period. The calculation of $\mathbf{K}$ and $\mathbf{f}$ can be respectively found in (4.7) and (4.10) in [33].

For FCS-MPC, there are only two switching state (corresponding $d = 1$ and $d = 0$). Each of the switching state gives rise to a different $i_{\mathrm{o}}(t+1)$ in the next sampling instant. If the prediction horizon exceeds one, the procedure replicates from $i_{\mathrm{o}}(t+1)$. Each of the switching state will lead to a new value of $i_{\mathrm{o}}(t+2)$ and so on [33].

To avoid the exponential growth of computational burden, the prediction horizon is set to 2, and the control horizon is 1. The corresponding cost function to be minimized is expressed as

$$J_{\mathrm{FCS}} = \left[i_{\mathrm{o}}\left(t+2|t\right) - I_{\mathrm{ref}}\right]^2. \tag{A4}$$

REFERENCES

[1] Y. Wang, J. Xu, Z. Chen, and F. Qin, “Small signal modeling and transient cross-regulation analysis of peak-current-mode-controlled SIDO buck LED driver,” *IEEE Trans. Power Electron.*, vol. 38, no. 10, pp. 12834–12845, Oct. 2023.

[2] Z. Dong, C. K. Tse, and S. Y. R. Hui, “Current-source-mode single-inductor multiple-output LED driver with single closed-loop control achieving independent dimming function,” *IEEE J. Emerg. Sel. Topics Power Electron.*, vol. 6, no. 3, pp. 1198–1209, Sep. 2018.

[3] F. Vasca and L. Iannelli Eds., *Dynamics and Control of Switched Electronic Systems: Advanced Perspectives For Modeling, Simulation and Control of Power Converters*. London, U.K.: Springer, 2012.

[4] Y. Wei, Q. Luo, S. Chen, J. Huang, and L. Zhou, “DC current bus distributed power system and its stability analysis,” *IET Power Electron*, vol. 12, no. 3, pp. 458–464, Mar. 2019.

[5] M. Tettamanti, F. Haller, A. Pidutti, P. D. Croce, and A. Baschirotto, “2.5A-constant-output-current, constant-T_{off}, 1.5 MHz, 89% -efficiency switching converter,” *IEEE Trans. Circuits Syst. II*, vol. 71, no. 3, pp. 1601–1605, Mar. 2024.

[6] M. Borage, S. Tiwari, and S. Kotaiah, “Analysis and design of an LCL-T resonant converter as a constant-current power supply,” *IEEE Trans. Ind. Electron.*, vol. 52, no. 6, pp. 1547–1554, Dec. 2005.

[7] X. Qu, S.-C. Wong, and C. K. Tse, “An improved LCLC current-source-output multistring LED driver with capacitive current balancing,” *IEEE Trans. Power Electron.*, vol. 30, no. 10, pp. 5783–5791, Oct. 2015.
[8] G. Wang and Y. W. Li, “Parabolic PWM for current control of voltage-source converters (VSCs),” *IEEE Trans. Ind. Electron.*, vol. 57, no. 10, pp. 3491–3496, Oct. 2010.
[9] Z. Shan, X. Ding, J. Jatskevich, and C. K. Tse, “Synthesis of multi-input multi-output DC/DC converters without energy buffer stages,” *IEEE Trans. Circuits Syst. II*, vol. 68, no. 2, pp. 712–716, Feb. 2021.
[10] J. H. Sun and K. W. E. Cheng, “Current-source mode switched-capacitor power converters with improved current gain capability,” *IET Power Electron*, vol. 13, no. 1, pp. 116–126, 2020.
[11] J. Sun, Y. C. Fong, and K. W. E. Cheng, “Current source mode bidirectional DC/DC converter with multiple-level output conversion ratios based on the hybrid PWM control of the switched-capacitor structure,” *IEEE J. Emerg. Sel. Topics Power Electron.*, vol. 10, no. 1, pp. 604–616, Feb. 2022.
[12] S. K, S. K, N. C, T. S. MSS, and S. K. B, “A single-inductor multi-output current-mode LED driver with soft-switching,” in *Proc. 1st Int. Conf. Elect., Electron., Inf. Commun. Technol.*, Feb. 2022, pp. 1–8.
[13] H. Zhang, D. Dong, M. Jing, W. Liu, and F. Zheng, “Topology derivation of multiple-port DC–DC converters based on voltage-type ports,” *IEEE Trans. Ind. Electron.*, vol. 69, no. 5, pp. 4742–4753, May 2022.
[14] W.-H. Yang, H.-A. Yang, C.-J. Huang, K.-H. Chen, and Y.-H. Lin, “A high-efficiency single-inductor multiple-output buck-type LED driver with average current correction technique,” *IEEE Trans. Power Electron.*, vol. 33, no. 4, pp. 3375–3385, Apr. 2018.
[15] X. L. Li, C. K. Tse, and D. D.-C. Lu, “Synthesis of reconfigurable and scalable single-inductor multiport converters with no cross regulation,” *IEEE Trans. Power Electron.*, vol. 37, no. 9, pp. 10889–10902, Sep. 2022.
[16] A. Zu, Q. Luo, J. Huang, Q. He, P. Sun, and X. Du, “Analysis and design of a multi-channel constant current LED driver based on DC current bus distributed power system structure,” *IET Power Electron*, vol. 13, no. 4, pp. 627–635, Mar. 2020.
[17] Z. Zhou, Y. Wang, C. Yanarates, and J. Macaulay, “Current sources and actual PV modules based photovoltaic (PV) emulator for testing MPPT algorithms and PV inverters,” in *Proc. IEEE 3rd Int. Conf. Ind. Electron. Sustain. Energy Syst.*, Jul. 2023, pp. 1–6.
[18] X. L. Li, Z. Dong, and C. K. Tse, “Series-connected current-source-mode multiple-output converters with high step-down ratio and simple control,” *IEEE Trans. Power Electron.*, vol. 34, no. 10, pp. 10082–10093, Oct. 2019.
[19] C. Liang et al., “Event-triggered MPC for current-source-mode single-inductor multiple-port DC-DC converter,” in *Proc. IEEE 14th Int. Symp. Power Electron. Distrib. Gener. Syst.*, Jun. 2023, pp. 932–937.
[20] R. Redl and J. Sun, “Ripple-based control of switching regulators—An overview,” *IEEE Trans. Power Electron.*, vol. 24, no. 12, pp. 2669–2680, Dec. 2009.
[21] H. Zhang, C. Yi, and P. Luo, “Current ripple recovery modeling technique for voltage-mode control converters,” *IEEE Trans. Circuits Syst. II*, vol. 65, no. 2, pp. 211–215, Feb. 2018.
[22] Z. Zhao, P. Luo, Z. Zhang, J. Fan, B. Zhang, and X. Chen, “A peak-valley current-mode buck converter with 3% to 95% duty cycle,” *IEEE Trans. Circuits Syst. II*, vol. 72, no. 1, pp. 328–332, Jan. 2025.
[23] J. Li and F. C. Lee, “Modeling of V^2 current-mode control,” *IEEE Trans. Circuits Syst. I*, vol. 57, no. 9, pp. 2552–2563, Sep. 2010.
[24] G. Zhou, J. Xu, and J. Wang, “Constant-frequency peak-ripple-based control of buck converter in CCM: Review, unification, and duality,” *IEEE Trans. Ind. Electron.*, vol. 61, no. 3, pp. 1280–1291, Mar. 2014.
[25] J. Cortes, V. Svikovic, P. Alou, J. A. Oliver, J. A. Cobos, and R. Wisniewski, “Accurate analysis of subharmonic oscillations of V^2 and V^2I_c controls applied to buck converter,” *IEEE Trans. Power Electron.*, vol. 30, no. 2, pp. 1005–1018, Feb. 2015.
[26] N. Ishraq and A. Mallik, “Small signal modeling of a four-level flying capacitor multilevel totem-pole PFC converter,” *IEEE Trans. Circuits Syst. I*, vol. 72, no. 4, pp. 1926–1938, Apr. 2025.
[27] F. Yu, F. C. Lee, and P. Mattavelli, “A small signal model for V^2 control with composite output capacitors based on describing function approach,” in *Proc. IEEE Energy Convers. Congr. Expo.*, Sep. 2011, pp. 1236–1243.
[28] D.-H. Shin, C. Jang, Y. Kim, T. T.-H. Kim, S. Lee, and K.-H. Baek, “An inductance-variation-insensitive buck converter using a dynamic ramp compensation with slope sensing technique,” *IEEE Trans. Circuits Syst. II*, vol. 71, no. 8, pp. 3700–3704, Aug. 2024.
[29] S. Tian, F. C. Lee, P. Mattavelli, and Y. Yan, “Small-signal analysis and optimal design of constant frequency V^2 control,” *IEEE Trans. Power Electron.*, vol. 30, no. 3, pp. 1724–1733, Mar. 2015.
[30] C. Bordons and C. Montero, “Basic principles of MPC for power converters: Bridging the gap between theory and practice,” *IEEE Ind. Electron. Mag.*, vol. 9, no. 3, pp. 31–43, Sep. 2015.
[31] M. Leng, G. Zhou, Q. Tian, G. Xu, and F. Blaabjerg, “Small signal modeling and design analysis for boost converter with valley V^2 control,” *IEEE Trans. Power Electron.*, vol. 35, no. 12, pp. 13475–13487, Dec. 2020.
[32] V. S. Ganesh and A. K. Singha, “Design of stable digital V^2 controllers for the synchronous noninverting buck–boost converter,” *IEEE J. Emerg. Sel. Topics Power Electron.*, vol. 11, no. 3, pp. 2826–2836, Jun. 2023.
[33] E. F. Camacho and C. Bordons, *Model Predictive Control*. London, U.K.: Springer, 2007.

Lunbo Deng (Member, IEEE) was born in Sichuan Province, China, in 1996. He received the B.Eng. degree in electrical engineering and automation in 2018, and the Ph.D. degree in electrical engineering in 2025, both from Southwest Jiaotong University, Chengdu, China.

From 2023 to 2024, he was a Visiting Ph.D. Student with the Department of Electrical and Computer Engineering at McMaster University, Hamilton, ON, Canada. He is currently a Postdoctoral Research Fellow with the College of Electrical Engineering, Zhejiang University, Hangzhou, China. His research interests include the modeling and control of power electronics system, integration of renewable energy and energy storage, and grid-connected converter technologies.

Guohua Zhou (Senior Member, IEEE) received the B.S. degree in electronic and information engineering and the M.S. and Ph.D. degrees in electrical engineering from Southwest Jiaotong University, Chengdu, China, in 2005, 2008, and 2011, respectively.

From March 2010 to September 2010, he was a Research Assistant with the Department of Electronic and Information Engineering, Hong Kong Polytechnic University, Hong Kong. From 2010 to 2011, he was a Visiting Scholar (also a Joint Ph.D. student) with the Center for Power Electronics Systems, Virginia Polytechnic Institute and State University, Blacksburg, VA, USA. He is currently a Professor with the School of Electrical Engineering, Southwest Jiaotong University. His current research interests include modulation and control techniques of power electronics systems, modeling and stability analysis of switching power converters, and renewable energy applications of power electronics.

Dr. Zhou was the recipient of the National Excellent Doctoral Dissertation of China in 2014. He was elected as a Fellow of the Institution of Engineering and Technology in 2018. He is currently an Associate Editor for *CPSS Transactions on Power Electronics and Applications.*